FIV2024
IGUAÇU FALLS, BRAZIL
2-5 JULY 2024

FIV2024: FSI² & FIV + N
10th International Symposium on Fluid-Structure Interactions,
Flow-Sound Interactions, Flow-Induced Vibration & Noise

FIV2024-0104
RESOLVENT ANALYSIS FOR AEROFOIL RESPONSE TO OPTIMAL GUSTS

Herman Mak
DAAA, ONERA, Institut Polytechnique de Paris, 92190 Meudon, France
herman.mak@onera.fr

Olivier Marquet
DAAA, ONERA, Université Paris Saclay, 92190 Meudon, France
olivier.marquet@onera.fr

Lutz Lesshafft
Laboratoire d'Hydrodynamique, CNRS, École Polytechnique, Institut Polytechnique de Paris, 91120 Palaiseau, France
lutz.lesshafft@polytechnique.edu

Abstract. *A flexible wing when encountering a gust has previously been shown to exhibit flutter despite being in a nominally stable pre-flutter regime. The classical approach to the analysis of gust response of a wing is to use a pre-defined perturbation in the experimental set-up. Instead, we propose using a technique common in non-modal linear fluid dynamics known as "resolvent analysis" in a coupled aeroelastic configuration to identify gust characteristics that cause an optimally high energy response in the wing in a linearly stable regime. The results from this method allow us to identify forcing and response modes which maximise a measure of energy of the response with respect to the energy of the forcing. We apply this technique on a 2D NACA 0012 aerofoil in laminar flow (Re = 1000) with heaving and pitching degrees of freedom. We choose to maximise the kinetic energy of structural oscillations for a fluid forcing input of unity norm, giving us a periodic forcing of the fluid that presents the most danger to the aerofoil structure. Our results show the structures of these gust forcings and the response of the aerofoil to these dangerous gusts. Moreover, the frequency of the forcing mode that optimally maximises the structural kinetic energy resonantly matches that of the least linearly stable eigenmode. This analysis therefore shows the potential for using resolvent analysis as a way to predict dangerous gusts.*

Keywords: *fluid-structure interactions, gust response, linear stability, resolvent analysis*

1. INTRODUCTION

An aeroplane can encounter sudden or periodic gusts of wind from both naturally occurring phenomena and wake-turbulence caused by other preceding aircraft. These gusts can cause flutter oscillations or divergence on a wing, which can lead to unwanted vibrations for the payload, discomfort for passengers, reduced aircraft performance and handling capabilities, and, in the worst case scenario, catastrophic failure of the wing. The critical parameters where these instabilities occur without gusts are usually investigated by means of linear stability analysis, whereby the stability of the aeroelastic operator is evaluated (Moulin and Marquet, 2021) (Negi *et al.*, 2020). However, instabilities have been shown to occur with wings even when the flow is in a linearly stable regime (Hémon *et al.*, 2006) (Schwartz *et al.*, 2009). On the other hand, a wing that is designed to reduce carbon emissions, with high span and minimal weight, will inevitably be more susceptible to these gusts due to its high bending moment and lower load-bearing capacity. It is therefore important to identify gusts that pose the greatest risk to a wing and to assess the response of the wing to the gust.

The classical approach to gust analysis is to purely characterise the response of the structural body to a pre-defined gust shape such as a sharp-edge or one-minus-cosine discrete gust, or a continuous gust based on a power spectral density function (Wu *et al.*, 2019) (Liauzun, 2010). However, we can instead utilise a technique often used in linear fluid dynamics problems known as *resolvent analysis* and apply its framework to aeroelastic problems with gust. This technique finds an input forcing mode and an output response mode that optimally maximises a gain in energy norm between the two modes in a linearly stable regime (Schmid, 2007). It was first applied to aeroelastic systems by Pfister *et al.* (2022) on a compliant wall patch in boundary layer flow. Applying this to our context allows us to instead identify a forcing in the fluid (a gust *per se*) that optimally excites the kinetic energy of the structure.

Additionally, Moulin and Marquet (2021) previously investigated linear instabilities of a flat plate with heaving and pitching degrees of freedom. Three possible modal instabilities were identified, known as vortex-induced-vibration (VIV), divergence, and flutter. There is a fourth nearly unstable mode they termed "anti-flutter". Flutter and anti-flutter are both

coupled modes, and the former has a heaving signal that lags the angle of attack signal, signifying it is extracting energy from the flow, whereas the latter has the opposite and as such is linearly stable.

2. TYPICAL SECTION MODEL

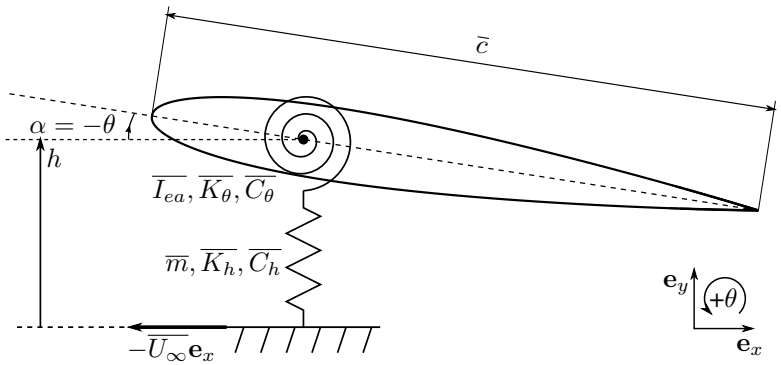

Figure 1. Schematic of an aerofoil with heaving and pitching degrees of freedom.

The response of a wing to gusts in a fluid flow is investigated based on the typical section model (Dowell *et al.*, 1980). Figure 1 shows the section of a NACA 0012 aerofoil of chord $\overline{c}$, mass $\overline{m}$ and moment of inertia $\overline{I_{ea}}$ about the elastic axis, which we choose to be located at the centre of gravity ($0.31\overline{c}$). Here, all dimensional quantities are denoted with $\overline{\times}$. In the typical section model, the aerofoil is mounted on two springs, a vertical spring $\overline{K_h}$ and a torsional spring $\overline{K_\theta}$, with two dampers characterised the damping coefficients $\overline{C_h}$ and $\overline{C_\theta}$ respectively. The motion of the aerofoil is described by vertical displacement h (heaving) and rotation angle θ with positive being in the clockwise direction (pitching) opposite to the angle of attack α. If we neglect the damping, then the oscillatory motion of the aerofoil in vacuum is characterised by the natural heaving and pitching frequencies defined as $\overline{\omega_{0,h}} = (\overline{K_h}/\overline{m})^{1/2}$ and $\overline{\omega_{0,p}} = (\overline{K_p}/\overline{I_{ea}})^{1/2}$ respectively. In the following analysis, the motion of the typical section will result from its interaction with the surrounding fluid characterised by the fluid density $\overline{\rho}$ and dynamic viscosity $\overline{\mu}$. The velocity of the flow upstream the typical section is uniform and equal to $\overline{U_\infty}$.

Hereinafter, all quantities are made non-dimensional using $\overline{c}$ as characteristic length, $\overline{c}/\overline{U_\infty}$ as characteristic time, and $\overline{\rho}\,\overline{c}^2$ as characteristic mass (per unit span). The typical section problem is then characterised by the following non-dimensional parameters:

$$Re = \frac{\overline{\rho}\overline{U_\infty}\,\overline{c}}{\overline{\mu}}\ ,\ \Omega = \frac{\overline{\omega_{0,h}}}{\overline{\omega_{0,p}}}\ ,\ \mathcal{U}^* = \frac{\overline{U_\infty}}{\overline{c}\,\overline{\omega_{0,p}}}\ ,\ \zeta_h = \frac{\overline{C_h}}{2\sqrt{\overline{m}\,\overline{K_h}}}\ ,\ \zeta_p = \frac{\overline{C_p}}{2\sqrt{\overline{I_{ea}}\,\overline{K_p}}}\ ,\ r_\theta = \sqrt{\frac{\overline{I_{ea}}}{\overline{m}\,\overline{c}^2}}\ ,\ m = \frac{\overline{m}}{\frac{1}{2}\overline{\rho}\,\overline{c}^2}. \quad (1)$$

The flow, being incompressible, is solely described by the Reynolds number *Re*. The structure is then characterised by the remaining non-dimensional parameters. Ω is the ratio between natural heaving and pitching frequencies. $\mathcal{U}^*$ is the reduced velocity which can be also expressed as $\mathcal{U}^* = 1/\omega_{0,p}$, i.e. the inverse of the non-dimensional heaving frequency $\omega_{0,p} = \overline{c}\,\overline{\omega_{0,p}}/\overline{U_\infty}$. ζ_h and ζ_p are the non-dimensional damping coefficient for heaving and pitching respectively. r_θ is the radius of gyration, and m is the solid to fluid mass ratio per unit span.

3. THEORETICAL AND NUMERICAL METHODS

3.1 GOVERNING NON-LINEAR EQUATIONS

In order to account for the rigid-body motion of the aerofoil, we follow the formalism of Mougin and Magnaudet (2002) applied to the typical section problem introduced by Moulin and Marquet (2021). In addition to the fixed coordinate system $(\mathbf{e}_x, \mathbf{e}_y)$ in the laboratory frame of reference, we introduce a non-inertial coordinate system $(\mathbf{e}_X(t), \mathbf{e}_Y(t))$ that rotates with the aerofoil. In this time-dependent frame, the velocity vector that is denoted $\mathbf{U}(\mathbf{X}, t) = [U, V]^T$ is related to the velocity vector $\mathbf{u} = [u, v]^T$ in the fixed frame by

$$\mathbf{U} = \mathbf{R}(\theta)^T\,\mathbf{u} \quad \text{where} \quad \mathbf{R}(\theta) = \begin{bmatrix} \cos\theta & -\sin\theta \\ \sin\theta & \cos\theta \end{bmatrix}, \quad (2)$$

here $\mathbf{R}(\theta)$ is the rotation matrix dependent on the angle θ. The variables used to describe the incompressible flow are gathered in the vector $\mathbf{q}_\mathrm{f} = [\mathbf{U}, P]^T$ where P denotes the scalar pressure field. The variables used to describe the

structural motion are gathered in the vector $\mathbf{q}_\mathrm{s} = [h, \theta, u_h, u_\theta]^T$ where $u_h = \mathrm{d}h/\mathrm{d}t$ and $u_\theta = \mathrm{d}\theta/\mathrm{d}t$ denotes the heaving and pitching velocities. Gathering solid and fluid vectors into a unique aeroelastic vector $\mathbf{q} = [\mathbf{q}_\mathrm{s}, \mathbf{q}_\mathrm{f}]^T$, the governing nonlinear equations can be formally written as

$$\begin{bmatrix} \mathbf{M}_\mathrm{s} & \mathbf{0} \\ \mathbf{0} & \mathbf{M}_\mathrm{f} \end{bmatrix} \frac{\partial \mathbf{q}}{\partial t} + \begin{bmatrix} \mathscr{R}_\mathrm{s}(\mathbf{q}_\mathrm{s}, \mathbf{q}_\mathrm{f}) \\ \mathscr{R}_\mathrm{f}(\mathbf{q}_\mathrm{s}, \mathbf{q}_\mathrm{f}) \end{bmatrix} = \begin{bmatrix} 0 \\ \mathbf{P}\mathbf{F} \end{bmatrix}, \tag{3}$$

where the first and second lines correspond to the solid and fluid equations respectively. On the right hand side, the momentum forcing vector $\mathbf{F} = [F_x, F_y]^T$ is introduced to model the gust in the flow. The operator $\mathbf{P}$ allows us to broadcast the forcing vector $\mathbf{F}$ in the momentum flow equation to the full flow state vector. The fluid mass matrix $\mathbf{M}_\mathrm{f}$ and residual vector $\mathscr{R}_\mathrm{f}$ are defined as

$$\mathbf{M}_\mathrm{f} = \begin{bmatrix} \mathbf{I}_2 & \\ & 0 \end{bmatrix}, \quad \mathscr{R}_\mathrm{f} = \begin{bmatrix} \mathbf{R}(\pi/2)\mathbf{U}u_\theta + \nabla\mathbf{U}(\mathbf{U} - \mathbf{W}) - \nabla \cdot \boldsymbol{\sigma}(\mathbf{U}, P) \\ \nabla \cdot \mathbf{U} \end{bmatrix}, \tag{4}$$

where the first term in the residual is a Coriolis-like acceleration induced by the rotation of the coordinate system. The fluid Cauchy stress tensor is classically defined as $\boldsymbol{\sigma}(\mathbf{U}, P) = -P\mathbf{I}_2 + Re^{-1}\left(\nabla\mathbf{U} + \nabla\mathbf{U}^T\right)$. In the convection term, $\mathbf{W}$ is the grid velocity defined as

$$\mathbf{W}(\theta, u_h, u_\theta; \mathbf{X}) = -\mathbf{R}(\theta)^T\mathbf{e}_x + \mathbf{R}(\theta)^T\mathbf{e}_y u_h + \mathbf{R}(\pi/2)\mathbf{X}u_\theta, \tag{5}$$

where $\mathbf{e}_x = [1, 0]^T$ and $\mathbf{e}_y = [0, 1]^T$. The first term is the velocity of the aerofoil in the $\mathbf{e}_x$ direction while the second term is the velocity of the aerofoil in the $\mathbf{e}_y$ direction. Both are expressed in the rotating frame of reference. The third term corresponds to the rotation velocity and depends on the position $\mathbf{X} = [X, Y]^T$ in the fluid domain. The flow equations are supplemented with the following boundary conditions. In the far field $\|\mathbf{X}\| \to \infty$, the velocity vanishes, i.e. $\mathbf{U} \to 0$. At the boundary of the aerofoil denoted Γ_w, the continuity of the fluid and solid is imposed, namely

$$\mathbf{U}(\mathbf{X}_w, t) = \mathbf{W}(\theta(t), u_h(t), u_\theta(t); \mathbf{X}_w), \tag{6}$$

where $\mathbf{X}_w = [X_w, Y_w]^T$ denotes the position on the aerofoil's wall. The solid mass matrix $\mathbf{M}_\mathrm{s}$ and residual vector $\mathscr{R}_\mathrm{s}$ in Eq. (3) are defined as

$$\mathbf{M}_\mathrm{s} = \begin{bmatrix} 1 & & & \\ & 1 & & \\ & & m & \\ & & & mr_\theta^2 \end{bmatrix}, \quad \mathscr{R}_\mathrm{s} = \begin{bmatrix} -u_h \\ -u_\theta \\ 2m\,\zeta_h \frac{\Omega}{\mathcal{U}^*} u_h + m\left(\frac{\Omega}{\mathcal{U}^*}\right)^2 h - C_l(\theta; \mathbf{U}, P) \\ 2(m\,r_\theta^2)\zeta_p \frac{1}{\mathcal{U}^*} u_\theta + (mr_\theta^2)\left(\frac{1}{\mathcal{U}^*}\right)^2 \theta - C_m(\mathbf{U}, P) \end{bmatrix}, \tag{7}$$

In the residual vector, C_l and C_m are the lift and moment coefficients defined in the rotating frame as

$$C_l(\theta; \mathbf{U}, P) = 2\left[\mathbf{R}(\theta)\int_{\Gamma_w} (\boldsymbol{\sigma}(\mathbf{U}, P) \cdot \mathbf{N})\right] \cdot \mathbf{e}_y, \quad \text{and} \quad C_m(\mathbf{U}, P) = 2\int_{\Gamma_w} (\mathbf{X} - \mathbf{X}_g) \times (\boldsymbol{\sigma}(\mathbf{U}, P) \cdot \mathbf{N}), \tag{8}$$

where $\mathbf{N}$ is the unit normal vector oriented towards the fluid domain and expressed in the rotating coordinate system. Drag coefficient C_d can also be calculated by replacing $\mathbf{e}_y$ with $\mathbf{e}_x$ in the equation for C_l. Since we are only considering the case where the elastic axis is at the centre of gravity, here $\mathbf{X}_g = \mathbf{0}$.

3.2 LINEAR AEROELASTIC ANALYSIS

From now, we assume that the gust is of infinitesimally small amplitude $\epsilon \ll 1$. The forcing term in Eq. (3) is replaced by $\epsilon\mathbf{F}'$. The fluid and solid variables are then expanded as the sum of a time-independent state and an infinitesimal perturbation given by

$$\begin{bmatrix} \mathbf{q}_\mathrm{s} \\ \mathbf{q}_\mathrm{f} \end{bmatrix} = \begin{bmatrix} \mathbf{q}_\mathrm{s}^B \\ \mathbf{q}_\mathrm{f}^B \end{bmatrix} + \epsilon \begin{bmatrix} \mathbf{q}_\mathrm{s}' \\ \mathbf{q}_\mathrm{f}' \end{bmatrix}, \tag{9}$$

where the steady state solution is denoted with superscript B while perturbations are denoted with $'$. Generally speaking, the time-independent solid component can be written $\mathbf{q}_\mathrm{s}^B = [\theta^B, 0, 0, 0]^T$ where θ^B is the negative of the static angle of attack. In the following, we will consider that this angle is strictly zero such that the solid component of the steady state vanishes, i.e. $\mathbf{q}_\mathrm{s}^B = \mathbf{0}$. Therefore, the steady state can be obtained by solely considering the steady flow equation

$$\begin{aligned} &\mathscr{R}_\mathrm{f}(\mathbf{0}, \mathbf{q}_\mathrm{f}^B) = \mathbf{0} \\ &\mathbf{U}^B(\mathbf{X}_w) = \mathbf{W}(0, 0, 0; \mathbf{X}_w), \end{aligned} \tag{10}$$

where the second line corresponds to the boundary conditions at the aerofoil's wall. According to Eq. (5), it reduces to $\mathbf{U}^B(\mathbf{X}_w) = [-1, 0]^T$ which is the velocity of the aerofoil expressed in a rotating but non-translating coordinate system. By injecting the decomposition Eq. (9) into Eq. (3), we obtain at order ϵ, after linearization around the steady state, the following equations that govern the aeroelastic perturbation

$$\begin{bmatrix} \mathbf{M}_\mathrm{s} & \mathbf{0} \\ \mathbf{0} & \mathbf{M}_\mathrm{f} \end{bmatrix} \frac{\partial}{\partial t} \begin{bmatrix} \mathbf{q}'_\mathrm{s} \\ \mathbf{q}'_\mathrm{f} \end{bmatrix} + \begin{bmatrix} \mathbf{J}_\mathrm{ss} & \mathbf{J}_\mathrm{sf} \\ \mathbf{J}_\mathrm{fs} & \mathbf{J}_\mathrm{ff} \end{bmatrix} \begin{bmatrix} \mathbf{q}'_\mathrm{s} \\ \mathbf{q}'_\mathrm{f} \end{bmatrix} = \begin{bmatrix} 0 \\ \mathbf{P}\mathbf{F}' \end{bmatrix}. \tag{11}$$

The blocks of the Jacobian matrix are obtained by linearising the residual vectors Eq. (4) and Eq. (7) around the steady state and are defined formally as $\mathbf{J}_{\mathrm{jk}} = \left.\frac{\partial \mathscr{R}_\mathrm{j}}{\partial \mathbf{q}_\mathrm{k}}\right|_{\mathbf{q}^B}$. For a complete description, we refer to Moulin and Marquet (2021) who performed a global stability analysis for a rectangular plate typical section with heaving and pitching degrees of freedom. In the next paragraph §3.2.1, we briefly lay out the global stability analysis before detailing in §3.2.2 the resolvent analysis introduced in the present study to investigate the response of the typical section to gusts.

3.2.1 GLOBAL STABILITY ANALYSIS

Global stability analysis is of interest when considering the growth or decay of self-sustained aeroelastic perturbations governed by Eq. (11) with the forcing term $\mathbf{F}' = \mathbf{0}$. The linear perturbation is then decomposed in the normal form

$$\begin{bmatrix} \mathbf{q}'_\mathrm{s}(t) \\ \mathbf{q}'_\mathrm{f}(\mathbf{X}, t) \end{bmatrix} = \begin{bmatrix} \hat{\mathbf{q}}_\mathrm{s} \\ \hat{\mathbf{q}}_\mathrm{f}(\mathbf{X}) \end{bmatrix} e^{\sigma t} + \text{c.c.} \tag{12}$$

where the temporal evolution of (complex) fluid-solid structures $[\hat{\mathbf{q}}_\mathrm{s}, \hat{\mathbf{q}}_\mathrm{f}]^T$ is assumed to be exponential, with the complex value $\sigma = \lambda + i\omega$ giving the growth rate λ and frequency ω. Here, c.c. indicates the complex conjugate. Introducing the above decomposition Eq. (12) into Eq. (11), we obtain the generalised eigenvalue problem

$$\begin{bmatrix} \mathbf{J}_\mathrm{ss} & \mathbf{J}_\mathrm{sf} \\ \mathbf{J}_\mathrm{fs} & \mathbf{J}_\mathrm{ff} \end{bmatrix} \begin{bmatrix} \hat{\mathbf{q}}_\mathrm{s} \\ \hat{\mathbf{q}}_\mathrm{f} \end{bmatrix} = -\sigma \begin{bmatrix} \mathbf{M}_\mathrm{s} & \mathbf{0} \\ \mathbf{0} & \mathbf{M}_\mathrm{f} \end{bmatrix} \begin{bmatrix} \hat{\mathbf{q}}_\mathrm{s} \\ \hat{\mathbf{q}}_\mathrm{f} \end{bmatrix} \tag{13}$$

showing that the complex fluid-solid structures are eigenmodes associated to the eigenvalue σ. To determine the aeroelastic stability of the steady state solution, we are interested in determining the eigenvalue of largest growth rate. The steady solution is globally stable when all the eigenvalues have negative growth rate, i.e $\lambda < 0$. The aeroelastic eigenvectors $[\hat{\mathbf{q}}_\mathrm{s}, \hat{\mathbf{q}}_\mathrm{f}]^T$ are normalised such that

$$\hat{\mathbf{q}}_\mathrm{s}^H \, \mathbf{M}_\mathrm{s} \, \hat{\mathbf{q}}_\mathrm{s} + \hat{\mathbf{q}}_\mathrm{f}^H \, \mathbf{M}_\mathrm{f} \, \hat{\mathbf{q}}_\mathrm{f} = 1, \tag{14}$$

where the superscript H denotes the conjugate transpose.

3.2.2 RESOLVENT ANALYSIS FOR OPTIMAL GUST

We now consider the gust problem for which the forcing term $\mathbf{F}' \neq \mathbf{0}$. We choose values of the non-dimensional parameters in Eq. (1) such that the steady state is globally stable. As the forced aeroelastic problem Eq. (11) is linear, the gust forcing and aeroelastic response can both be decomposed in temporal Fourier modes as follows,

$$\mathbf{F}'(\mathbf{X}, t) = \tilde{\mathbf{F}}(\mathbf{X}) e^{i\omega_f t} + \text{c.c.} \quad \text{and} \quad \begin{bmatrix} \mathbf{q}'_\mathrm{s}(t) \\ \mathbf{q}'_\mathrm{f}(\mathbf{X}, t) \end{bmatrix} = \begin{bmatrix} \tilde{\mathbf{q}}_\mathrm{s} \\ \tilde{\mathbf{q}}_\mathrm{f}(\mathbf{X}) \end{bmatrix} e^{i\omega_f t} + \text{c.c.} \tag{15}$$

where the real parameter ω_f is the frequency of the forcing defined by its (complex) spatial shape $\tilde{\mathbf{F}}(\mathbf{X})$. The aeroelastic response that also oscillates at the frequency ω_f is characterised by its (complex) solid $\tilde{\mathbf{q}}_\mathrm{s}$ and fluid $\tilde{\mathbf{q}}_\mathrm{f}$ components. Introducing the harmonic decomposition Eq. (15) into Eq. (11), we obtain the following input-output relation between the forcing and aeroelastic response structures

$$\underbrace{\left(i\omega_f \begin{bmatrix} \mathbf{M}_\mathrm{s} & \mathbf{0} \\ \mathbf{0} & \mathbf{M}_\mathrm{f} \end{bmatrix} + \begin{bmatrix} \mathbf{J}_\mathrm{ss} & \mathbf{J}_\mathrm{sf} \\ \mathbf{J}_\mathrm{fs} & \mathbf{J}_\mathrm{ff} \end{bmatrix} \right)}_{\boldsymbol{\mathcal{R}}(\omega_f)} \underbrace{\begin{bmatrix} \tilde{\mathbf{q}}_\mathrm{s} \\ \tilde{\mathbf{q}}_\mathrm{f} \end{bmatrix}}_{\tilde{\mathbf{q}}} = \underbrace{\begin{bmatrix} 0 \\ \mathbf{P} \end{bmatrix}}_{\mathcal{P}} \tilde{\mathbf{F}}. \tag{16}$$

$\boldsymbol{\mathcal{R}}(\omega_f)$ is commonly termed the *resolvent operator*. If the gust shape $\tilde{\mathbf{F}}$ is prescribed, this input-ouput relation allows us to directly solve for the linear aeroelastic response $\tilde{\mathbf{q}}$. However, we are instead interested in determining the most dangerous gusts which we will define here as a gust that induces the highest kinetic energy response of the typical section. To that aim, we start by defining the ratio

$$G(\tilde{\mathbf{F}}; \omega_f) = \frac{m(\tilde{u}_h^* \tilde{u}_h) + m r_\theta^2 (\tilde{u}_p^* \tilde{u}_p)}{\int_{\Omega_f} \tilde{\mathbf{F}}^* \cdot \tilde{\mathbf{F}}}$$

where the numerator is the kinetic energy of the solid structure (output) and the denominator is a norm of the gust (input) in an arbitrary spatial domain Ω_f. After spatial discretisation of the operators,this ratio can be reformulated as

$$G = \frac{\tilde{\mathbf{q}}^H \mathbf{M}_\mathrm{o} \tilde{\mathbf{q}}}{\tilde{\mathbf{F}}^H \mathbf{M}_\mathrm{i} \tilde{\mathbf{F}}} \quad , \text{ where } \quad \mathbf{M}_\mathrm{o} = \begin{bmatrix} \mathbf{M}_\mathrm{SKE} & \\ & \mathbf{0} \end{bmatrix} \quad \text{and} \quad \mathbf{M}_\mathrm{SKE} = \begin{bmatrix} 0 & & & \\ & 0 & & \\ & & m & \\ & & & m r_\theta^2 \end{bmatrix}, \tag{17}$$

where $\mathbf{M}_\mathrm{i}$ is the mass matrix from discretisation of the spatial integral of the input forcing, and the aeroelastic perturbation satisfies Eq. (16). By injecting that relation into Eq. (17), we obtain the eigenvalue problem

$$\left(\mathcal{P}^H \boldsymbol{\mathcal{R}}(\omega_f)^H \mathbf{M}_\mathrm{o} \boldsymbol{\mathcal{R}}(\omega_f) \mathcal{P}\right) \tilde{\mathbf{F}}_k = G_k \mathbf{M}_\mathrm{i} \tilde{\mathbf{F}}_k, \tag{18}$$

where $\tilde{\mathbf{F}}_k$ are eigenvectors associated to eigenvalues G_k. Given the operator on the left hand side is hermitian, the eigenvalues are necessarily real and positive, and can be ordered as $G_0 \geq G_1 \geq G_2 \geq \cdots \geq 0$. The optimal gust is therefore given by $\tilde{\mathbf{F}}_0$. The aeroelastic state $\tilde{\mathbf{q}}_k$ corresponding to the forcing mode $\tilde{\mathbf{F}}_k$ are obtained by solving the harmonic problem Eq. (16). In fact, solving the above eigenvalue problem is equivalent to solving for a singular value decomposition of the resolvent operator $\mathcal{R}(\omega)$ with singular values G_k associated to the right singular modes $\hat{\mathbf{F}}_k$ and the left singular modes $\hat{\mathbf{q}}_k$.

3.3 NUMERICAL APPROACH

The incompressible Navier-Stokes equations are discretised in space using the finite element method with grad-div stabilisation in the fluid momentum equations with a constant coefficient $\gamma = 1$ to improve the enforcement of the divergence-free condition (Olshanskii *et al.*, 2009). The weak form of the equations is implemented in Python using the FEniCSx (version 0.6.0) library (Baratta *et al.*, 2023). The boundary condition Eq. (6) at the aerofoil's wall is implemented in the weak form by introducing a Lagrange multiplier unknown (Pfister *et al.*, 2022) that is also used to assess the aerodynamic lift and drag coefficients in Eq. (8). This was implemented via an additional library known as multiphenicsx (Ballarin, 2024) which allows us to define integrals on certain parts of the domain (in this case the aerofoil wall boundary). The inlet, upper, and lower far-field boundaries were strongly imposed to have zero velocity, and a stress-free boundary condition is imposed at the outlet boundary. The steady base-state is solved using the Newton method implemented in petsc4py (Dalcin *et al.*, 2011) by repeated inversion of the Jacobian using MUMPS (Amestoy *et al.*, 2001) for the LU solver. The linear stability analysis is conducted with the additional layer of slepc4py (Hernandez *et al.*, 2005) using a shift-invert method to find eigenvalues and corresponding eigenmodes near the imaginary axis. We validated the implementation of the steady base-state and linear stability analysis against the work of Moulin and Marquet (2021) by using a mesh provided by the authors and removing SUPG stabilisation in their source code and comparing their results with ours. Resolvent analysis is then again implemented with slepc4py by searching for the greatest magnitude eigenvalue for each desired value of ω_f. For this part of the analysis, we did not explicitly numerically assemble the resolvent matrix, but instead used PETSc's "matrix-free" capability to invert the matrix.

In order to make the forcing resemble an incoming gust, we also chose to mask the forcing by multiplying the prolongation matrix $\mathbf{P}$ by a function $(1-\tanh(3X+2))/2$ which smoothly steps down from 1 to 0 in the stream-wise direction at a distance of $2c/3$ in front of the aerofoil. This, in effect, limits the optimised gust to only in front of the aerofoil.

4. RESULTS

We numerically investigated the aeroelastic response of a NACA 0012 aerofoil to gust modelled as an harmonic forcing. In the present study, most of the non-dimensional parameters that characterises this aeroelastic problem (see Eq. (1)) are fixed to the following values

$$Re = 1000, \quad \Omega = 0.8, \quad \zeta_h = 0.0067, \quad \zeta_p = 0.05, \quad r_\theta = 0.289, \quad m = 1000 \tag{19}$$

They are similar to those used by Moulin and Marquet (2021) who performed the aeroelastic stability analysis of a rectangular plate in a laminar flow. The low value of the Reynolds number ensures that the flow around the rigid aerofoil is time-independent. The structural parameters are chosen similarly to the experimental study by Amandolese *et al.* (2013). The value of the solid-fluid mass ratio m corresponds approximately to a 1 metre long stainless steel aerofoil in air. The effect of the reduced velocity $\mathcal{U}^*$ on the aeroelastic dynamics is investigated by varying its value in the range $[10^{-2}, 10^{1}]$.

For this numerical study, the computational domain used to discretise the flow equations around the NACA 0012 aerofoil is rectangular. The inlet boundary is located 20 chord lengths before the leading edge. The outlet boundary is located 25 chord lengths behind the leading edge. The upper and lower boundaries are set at 20 chord lengths above and below the leading edge respectively.The unstructured mesh made of 255 624 triangles is obtained with the GMSH

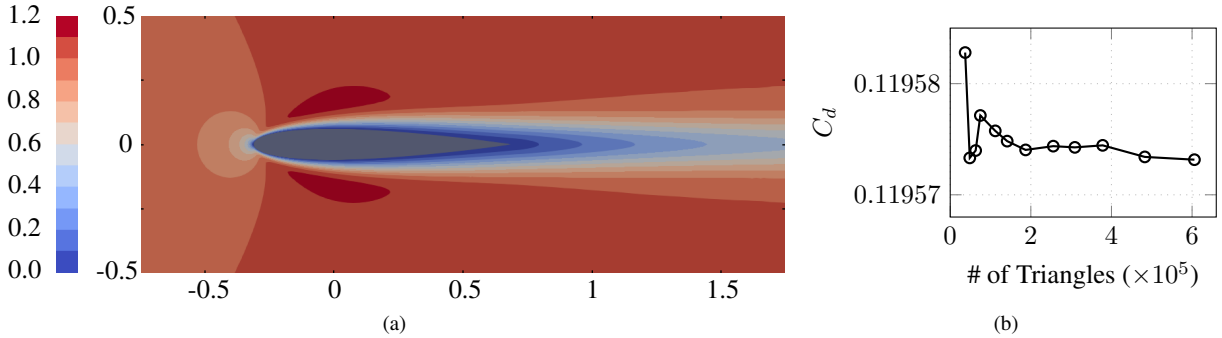

(a) (b)

Figure 2. (a) Stream-wise velocity u^B of the steady flow around the NACA 0012 aerofoil at $Re = 1000$ and $\alpha = 0°$. The origin is located at the elastic axis/centre of gravity at $0.31c$. (b) Steady-state drag coefficient C_d as a function of the number of triangles in different meshes.

library. The aerofoil wall itself is made up of 1 334 points. Figure 2(a) displays the stream-wise velocity of the steady flow around the aerofoil at $Re = 1000$ for the angle $\alpha = 0°$. Note that the velocity displayed here is the velocity of the time-independent frame rather than the direct output from calculations in the time-dependent frame. As expected, the flow is symmetric with respect to the y-axis. For this low-Reynolds number, a thick laminar boundary layer develops around the aerofoil and remains attached up to the trailing edge. The size of the wake developing downstream the aerofoil is similar to the thickness of the aerofoil. The drag coefficient C_d is reported in Figure 2(b) as a function of the number of triangles for different mesh refinements. The variation is of order 10^{-6} and converges at around 2×10^5 triangles, showing that the reported steady flow is independent of the chosen mesh.

4.1 STABLE AND UNSTABLE REGIMES WITH GLOBAL STABILITY ANALYSIS

To determine the linearly stable and unstable aeroelastic regimes, a global stability analysis of the spring-mounted aerofoil described in §3.2.1 is first performed for the steady flow described above with the parameters given in Eq. (19). Figure 3(a) displays a typical eigenvalue spectrum obtained by computing leading eigenvalues of Eq. (13) for the reduced velocity $\mathcal{U}^* = 8.5$. There are two eigenvalues with nearly positive growth rate ($\lambda \lesssim 0$) that are highlighted in blue and red. The rest of the eigenvalues are much more stable and correspond to spurious modes that do not contribute to the physics of the problem. The eigenmode associated to the eigenvalue of largest growth rate corresponds to the *flutter* mode described in Moulin and Marquet (2021) and will be labelled in blue for all following figures. The heaving signal (h') lags the angle of attack signal ($\alpha' = -\theta'$) which implies that energy is transferred from the fluid flow to the structure. As long as the mode is stable, the energy transfer is not enough to counterbalance the structural dissipation given by damping ζ_h and ζ_p. The eigenmode associated to the second least-stable eigenvalue is labelled in red, and corresponds to the *anti-flutter* mode described in Moulin and Marquet (2021), where the heaving signal leads the angle of attack signal. Since the energy is transferred from the structure to the flow, the flow tends to dissipate the energy of the structure.

For the unstable flat plate of Moulin and Marquet (2021), the flutter frequency matches that of the natural heaving frequency, and the anti-flutter mode frequency is in between the natural heaving and natural pitching frequencies. The frequency of the anti-flutter mode for the slightly stable aerofoil is $\omega_{\text{anti}} = 0.0945$, which, unlike the unstable flat plate, is closer to the natural heaving frequency $\omega_{0,h} = \Omega/\mathcal{U}^* = 0.0941$ than the frequency of the flutter mode $\omega_{\text{flut}} = 0.0987$, which is in between the natural heaving and pitching frequency $\omega_{0,p} = 1/\mathcal{U}^* = 0.1176$ albeit much more closer to the former.

These two eigenvalues were also tracked while varying the reduced velocity $\mathcal{U}^*$. The evolution of their growth rates and frequencies is displayed in Fig. 3(b). The flutter mode (blue) becomes less stable as the reduced velocity increases and becomes unstable for some critical reduced velocity $\mathcal{U}^* \geq \mathcal{U}^*_c = 9.84$. On the other hand, the anti-flutter mode (red) becomes more stable as $\mathcal{U}^*$ increases. Interestingly, at $\mathcal{U}^* = 7.94$, the growth rate of the flutter and anti-flutter mode cross and their frequencies nearly coincide as well. In fact, at lower reduced velocities, the angle of attack signal for both eigenmodes lags behind the heaving signal. As such, both modes are characterised by a positive transfer of energy from the structure to the fluid. Therefore, the distinction between flutter and anti-flutter modes is no longer physically relevant for $\mathcal{U}^* \leq 7.94$. In fact, from that point, as we decrease $\mathcal{U}^*$, the frequency of the red anti-flutter mode converges towards the natural pitching frequency, and the flutter mode frequency converges towards the natural heaving frequency.

4.2 AEROELASTIC RESPONSE TO OPTIMAL GUST USING RESOLVENT ANALYSIS

We investigate how gusts affect the two regimes found in §4.1 by first performing resolvent analysis on a single value within each regime. Figure 4(a) and 4(b) shows the optimal and sub-optimal gain (G_0, G_1 respectively) with respect to frequency ω_f for a case in the region where the anti-flutter mode is least stable ($\mathcal{U}^* = 7.0$) and in the region where the

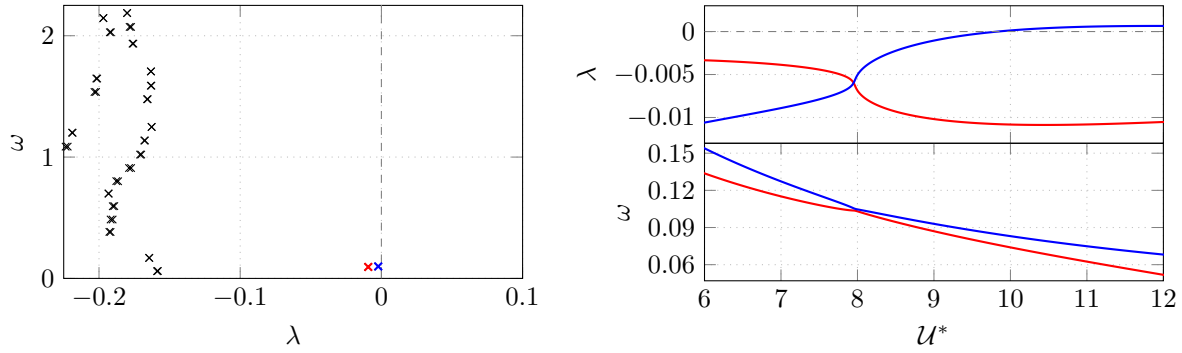

(a) (b)

Figure 3. Results of global stability analysis. (a) Eigenvalue spectrum at $\mathcal{U}^* = 8.5$. (b) Real [upper] and imaginary [lower] parts of the two leading eigenvalues as a function of $\mathcal{U}^*$. Marginal stability ($\lambda = 0$) is indicated with a (- -) line. The critical reduced velocity is $\mathcal{U}^*_c = 9.84$. Eigenvalues associated with flutter and anti-flutter modes (at $\mathcal{U}^* = 8.5$) are highlighted in blue and red respectively.

flutter mode is the least stable mode ($\mathcal{U}^* = 8.5$). We see that they both have a single optimal gain peak, and it is located at the nearly the same frequency as that of the least stable mode in each case. Moreover, we see that in both cases, the sub-optimal gain is orders of magnitudes smaller than the peak optimal gain.

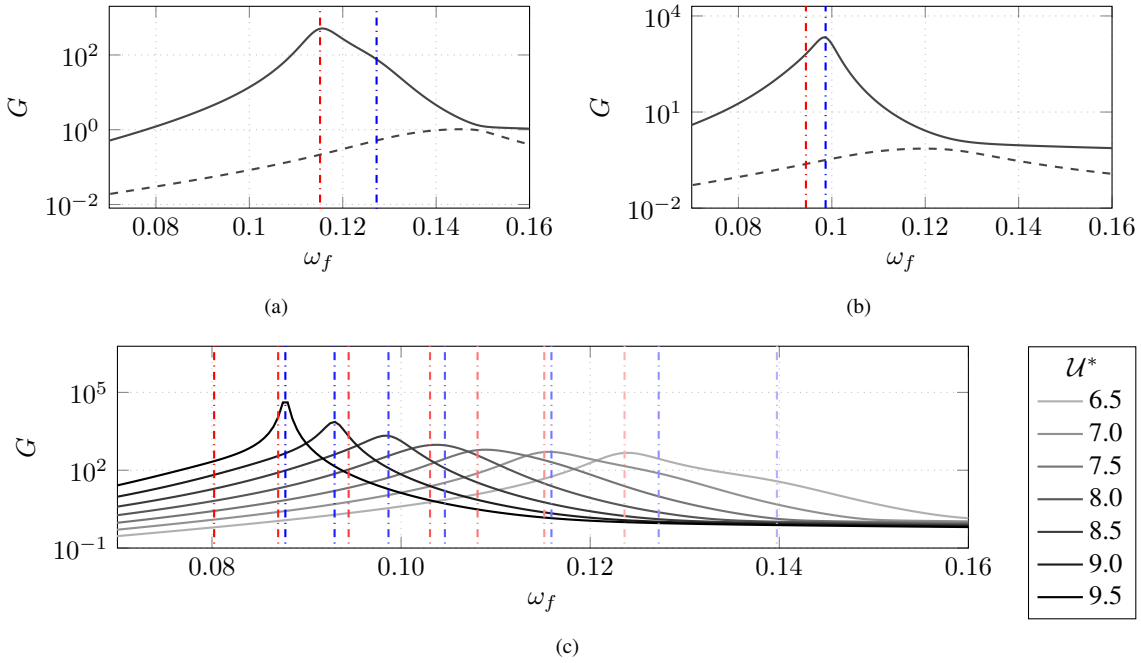

(a) (b)

(c)

Figure 4. Optimal (–) and first sub-optimal (- -) resolvent energy gains at (a) $\mathcal{U}^* = 7$ and (b) $\mathcal{U}^* = 8.5$. (b) Optimal resolvent energy gains at a range of values of $\mathcal{U}^*$. The angular frequency of flutter and anti-flutter modes from stability analysis are indicated by blue and red ($-\cdot$) lines respectively.

Figure 4(c) shows the optimal gain and flutter/anti-flutter frequencies of several values of $\mathcal{U}^*$. We can observe that for values of stable $\mathcal{U}^*$ where the flutter mode is least stable, the optimal gain peaks match with the flutter mode's frequency. And where the anti-flutter mode is least stable, the optimal gain peaks match with the anti-flutter mode's frequency. This gives the intuitive result that a gust with a frequency equal to flutter resonates with a nearly unstable flutter mode.

Snapshots of a half-period of the stream-wise component of the forcing mode and pressure/displacement perturbation of the response mode at the optimal gain peak for $\mathcal{U}^* = 7.0$ and $\mathcal{U}^* = 8.5$ are shown in Fig. 5 and Fig. 6 respectively. Both forcing modes are anti-symmetric about the mean chord line and are concentrated around the mean chord line. Of particular note is that the response in Fig. 6 matches extremely well with the flutter eigenmode of stability analysis (not shown).

Moreover, the heaving and pitching signals of these two optimal gain peak responses were plotted in Fig. 7. In both regimes, the responses have a heaving signal that lags the angle of attack signal, signifying that energy is being transferred from the fluid to the solid. The phase difference between the two signals of the optimal response matches that of the flutter

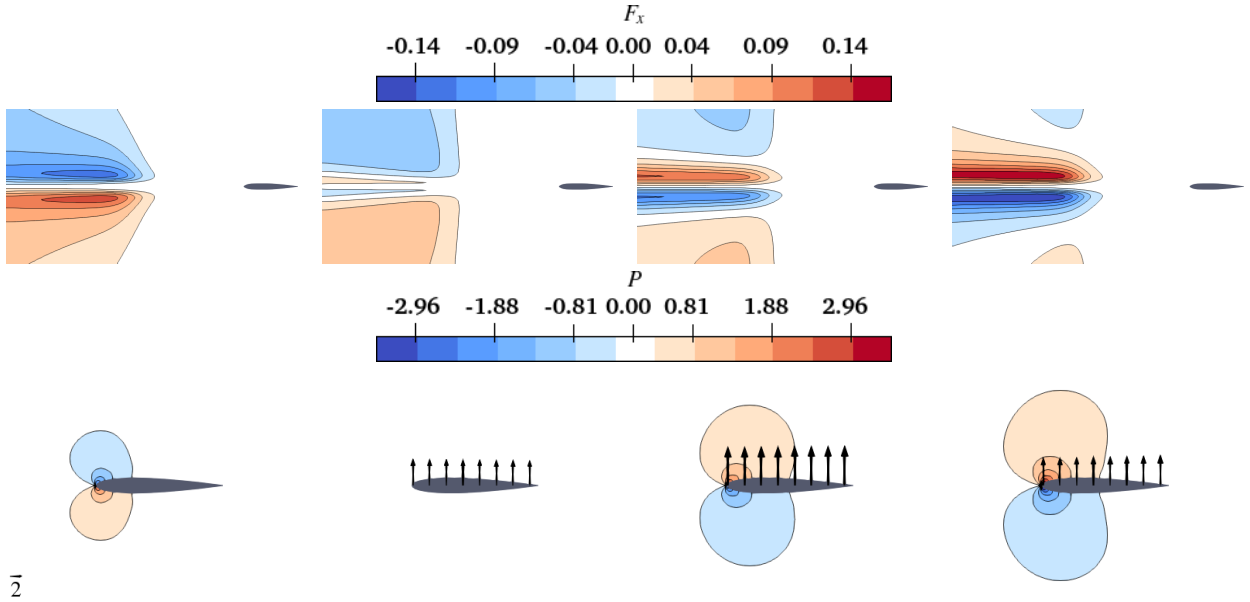

$\vec{2}$

Figure 5. Snapshots of a half-period of the optimal [top] stream-wise forcing and [bottom] pressure/displacement perturbation of the response at $\omega t \approx \{0, \pi/4, \pi/2, 3\pi/4\}$ for $\mathcal{U}^* = 7$.

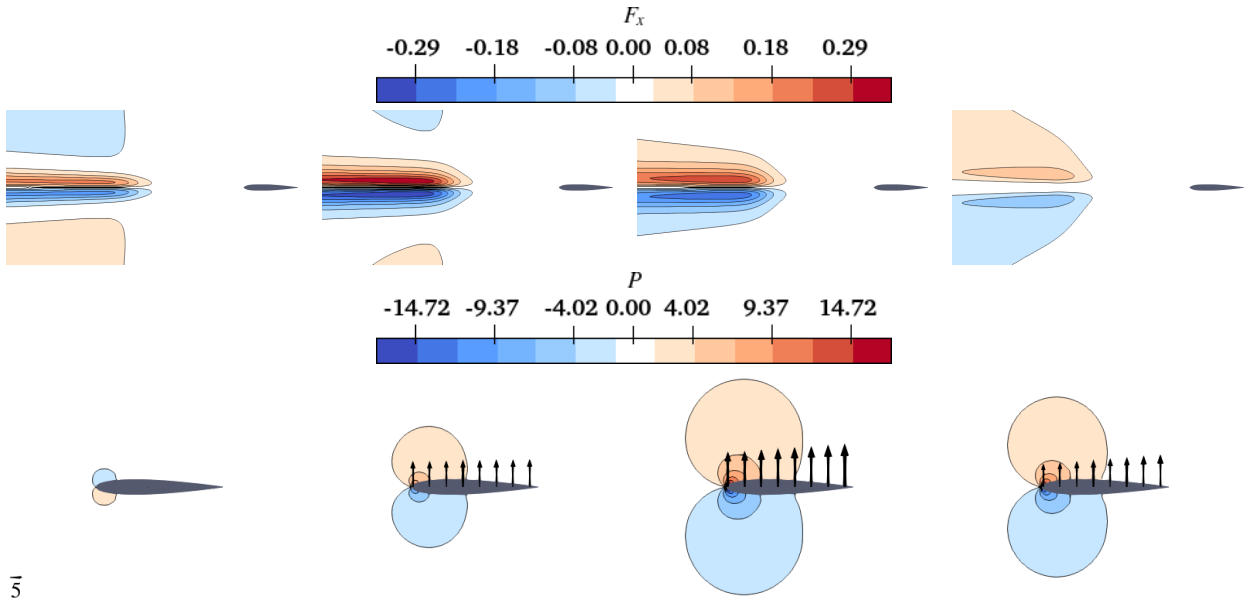

$\vec{5}$

Figure 6. Snapshots of a half-period of the optimal [top] stream-wise forcing and [bottom] pressure/displacement perturbation of the response at $\omega t \approx \{0, \pi/4, \pi/2, 3\pi/4\}$ for $\mathcal{U}^* = 8.5$.

mode for $\mathcal{U}^* = 8.5$. Whereas the phase difference of the optimal response at $\mathcal{U}^* = 7.0$ does not match that of the anti-flutter mode. This suggests that despite the frequency of the anti-flutter mode matching with the frequency of the optimal gain peak, the response is not that of anti-flutter and is perhaps a combination of modes. We can also see here that ratio between the amplitude of pitching in comparison to heaving is less than that of the flutter response mode. This is also visible when viewing displacements in the response snapshots in Fig. 5, where there is very little variation in angle of attack. Thus, at this lower reduced velocity, the gust response is mostly a heaving mode, possibly due to the relatively low heaving damping coefficient.

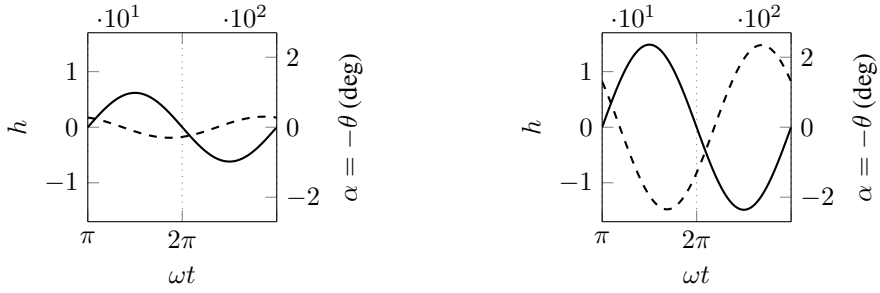

(a) $\mathcal{U}^* = 7$ (b) $\mathcal{U}^* = 8.5$

Figure 7. Heaving h position (–) and pitching angle of attack α (- -) over one period of the optimal gain peak response.

5. CONCLUSION

Global linear stability analysis and resolvent analysis were conducted on a heaving/pitching NACA 0012 aerofoil section to determine gusts dangerous to a wing in a linearly stable regime and to assess how the wing responds to the gusts. The aerofoil was found to be globally stable at reduced velocities lower than a certain critical value. The mode that reaches instability above that threshold is a coupled-mode flutter. Tracing the mode through decreasing reduced velocity reveals that there are two distinct regimes separated by the point where the two leading eigenvalues nearly coincide. At reduced velocities lower than that threshold, the leading mode is no longer flutter as the transfer of energy no longer goes from the fluid to the solid.

Where the aeroelastic system is globally stable, conducting resolvent analysis allowed us to see the frequency and structure of a gust that optimally excites the kinetic energy of the aerofoil, as well as the aerofoil's response to the gust. In the two stable regimes, the frequencies of these resolvent modes matched that of the least stable eigenmodes. However, the structure of the modes only matched when the flutter mode was the least stable mode, suggesting an interaction of modes in the other regime. Further work can be done to further analyse the response of the aerofoil. The tools used here serve as an example for possible future exploration of gusts and responses to gusts in other configurations. These include gusts in more realistic three-dimensional flows as well as in higher Reynolds numbers flows where turbulence modelling would be necessary.

ACKNOWLEDGEMENTS

We thank Dr Johann Moulin for his early contributions to this project. This work was funded by ONERA and DGAC via the project ALFA (Active control for Low-Fuel consumption Aircraft).

REFERENCES

Amandolese, X., Michelin, S. and Choquel, M., 2013. "Low speed flutter and limit cycle oscillations of a two-degree-of-freedom flat plate in a wind tunnel". *Journal of Fluids and Structures*, Vol. 43, pp. 244–255.

Amestoy, P.R., Duff, I.S., Koster, J. and L'Excellent, J.Y., 2001. "A fully asynchronous multifrontal solver using distributed dynamic scheduling". *SIAM Journal on Matrix Analysis and Applications*, Vol. 23, No. 1, pp. 15–41.

Ballarin, F., 2024. "Multiphenicsx - easy prototyping of multiphysics problems in FEniCSx". https://multiphenics.github.io/.

Baratta, I.A., Dean, J.P., Dokken, J.S., Habera, M., Hale, J.S., Richardson, C.N., Rognes, M.E., Scroggs, M.W., Sime, N. and Wells, G.N., 2023. "DOLFINx: the next generation FEniCS problem solving environment". preprint. doi: 10.5281/zenodo.10447666.

Dalcin, L.D., Paz, R.R., Kler, P.A. and Cosimo, A., 2011. "Parallel distributed computing using Python". *Advances in Water Resources*, Vol. 34, No. 9, pp. 1124–1139. ISSN 0309-1708. doi:10.1016/j.advwatres.2011.04.013.

Dowell, E.H., Curtiss, H., Scanlan, R.H. and Sisto, F., 1980. "A modern course in aeroelasticity". *Sijthoff & Noordhoff, Alphen aan den Rijn, The Netherlands*.

Hémon, P., de Langre, E. and Schmid, P., 2006. "Experimental evidence of transient growth of energy before airfoil flutter". *Journal of Fluids and Structures*, Vol. 22, No. 3, pp. 391–400.

Hernandez, V., Roman, J.E. and Vidal, V., 2005. "SLEPc: A scalable and flexible toolkit for the solution of eigenvalue problems". *ACM Transactions on Mathematical Software*, Vol. 31, No. 3, pp. 351–362. ISSN 0098-3500. doi: 10.1145/1089014.1089019.

Liauzun, C., 2010. "Aeroelastic Response to Gust Using CFD Techniques". In *ASME 2010 7th International Symposium on Fluid-Structure Interactions, Flow-Sound Interactions, and Flow-Induced Vibration and Noise: Volume 3, Parts A and B*. ASMEDC, Montreal, Quebec, Canada, pp. 269–276. ISBN 978-0-7918-5451-8. doi:10.1115/FEDSM-ICNMM2010-30153.

Mougin, G. and Magnaudet, J., 2002. "The generalized Kirchhoff equations and their application to the interaction between a rigid body and an arbitrary time-dependent viscous flow". *International Journal of Multiphase Flow*, Vol. 28, No. 11, pp. 1837–1851.

Moulin, J. and Marquet, O., 2021. "Flow-induced instabilities of springs-mounted plates in viscous flows: A global stability approach". *Physics of Fluids*, Vol. 33, No. 3, p. 034133.

Negi, P.S., Hanifi, A. and Henningson, D.S., 2020. "On the linear global stability analysis of rigid-body motion fluid–structure-interaction problems". *Journal of Fluid Mechanics*, Vol. 903, p. A35. ISSN 0022-1120, 1469-7645. doi:10.1017/jfm.2020.685. URL `https://www.cambridge.org/core/product/identifier/S0022112020006850/type/journal_article`.

Olshanskii, M., Lube, G., Heister, T. and Löwe, J., 2009. "Grad–div stabilization and subgrid pressure models for the incompressible Navier–Stokes equations". *Computer Methods in Applied Mechanics and Engineering*, Vol. 198, No. 49-52, pp. 3975–3988. ISSN 00457825. doi:10.1016/j.cma.2009.09.005. URL `https://linkinghub.elsevier.com/retrieve/pii/S004578250900303X`.

Pfister, J.L., Fabbiane, N. and Marquet, O., 2022. "Global stability and resolvent analyses of laminar boundary-layer flow interacting with viscoelastic patches". *Journal of Fluid Mechanics*, Vol. 937, p. A1.

Schmid, P.J., 2007. "Nonmodal Stability Theory". *Annual Review of Fluid Mechanics*, Vol. 39, No. 1, pp. 129–162.

Schwartz, M., Manzoor, S., Hémon, P. and de Langre, E., 2009. "By-pass transition to airfoil flutter by transient growth due to gust impulse". *Journal of Fluids and Structures*, Vol. 25, No. 8, pp. 1272–1281.

Wu, Z., Cao, Y. and Ismail, M., 2019. "Gust loads on aircraft". *The Aeronautical Journal*, Vol. 123, No. 1266, pp. 1216–1274.